Supporting Information

for

Segmental and interfacial dynamics quantitatively determine ion transport in solid polymer composite electrolytes

Yage. Huang[1], Xintong. Mei[1], Prof. Yunlong. Guo[1]

[1]University of Michigan – Shanghai Jiao Tong University Joint Institute, Shanghai Jiao Tong University, Shanghai 200240, China.

E-mail: yunlong.guo@sjtu.edu.cn

Content

1. Additional experimental methods 3

2. Microstructure and composition of PCE 6

2.1 Nano CT Imaging 6

2.2 TGA 11

2.3 FTIR 15

3. Percolation theory 17

4. Crystallization behavior 19

5. Mechanical characterization 24

6. Li^+ transference number 25

7. Dynamics 27

7.1 Identification of region boundaries 27

7.2 Fitting procedures 30

7.3 Correlation between Z^* and ε^* 32

7.4 Sensitivity of relaxation time to conductivity 33

7.5 VFT plots 35

7.6 Supplementary data of α_2 process 37

7.7 Coupling between relaxation processes 41

REFERENCES 44

1. Additional experimental methods

1.1 Nano CT Imaging. Three-dimensional (3D) scanning of the samples was performed by an X-ray computed tomography (CT) scanner: ZEISS Xradia 520 Versa with highest resolution of 700 nm. The membrane sample was cut to planar dimensions of 1 mm × 1 mm, required by the equipment. As output of the Nano CT, 3D images were digitalized and reconstructed at a given resolution of 1 μm. Data were further analyzed to get the average size and volume percentage of LLZTO/SiO_2 particles or particle clusters.

1.2 Differential Scanning Calorimetry (DSC). Crystallinity has remarkedly impact on ion transport. To maintain a certain processing method of the PCE, a constant crystallization temperature (T_c) was chosen for further EIS characterization. Prior to the selection, effect of T_c on crystallinity was examined by crystallization kinetic analysis. Isothermal crystallization kinetics was carried out by a Shimadzu DSC-60 plus DSC under nitrogen atmosphere. The instrument was calibrated by indium. The sample was heated to 80 ℃ with a constant ramp rate of 10 ℃/min and annealed thereat for 10 min to ensure that it melted completely, and then quenched to a T_c, 20 ℃, 30 ℃ or 50 ℃ to crystallize isothermally for various times. Temperature protocol used in crystallization testing and the resulting heat flow traces for representative samples are shown in Figure S1 and Figure S9, respectively.

The crystallinity (X_t) of the composite is calculated by:

$$X_t = \frac{\Delta H_m}{\Delta H_{PEO} f_{PEO}} \tag{S1}$$

where X_t is the crystallinity of PEO, ΔH_m is the melting enthalpy of the composite, ΔH_{PEO} is the value of melting enthalpy for PEO having completely crystallized (203 $J \cdot g^{-1}$)(Ref. [1]) and f_{PEO} is the mass fraction of PEO in the composite.

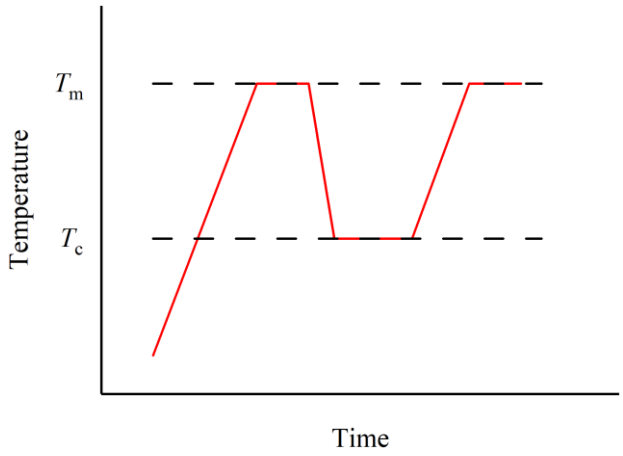

Figure S1. Temperature protocol of crystallization test.

1.3 Fourier Transform Infrared Spectroscopy (FTIR). FTIR spectra were recorded on Nicolet 6700 at room temperature. Spectral resolution was $2cm^{-1}$.

1.4 Thermal Gravimetric Analyzer (TGA). Bulk compositional analysis of the composite was carried out using a TA Instruments thermal gravimetric analyzer (SDT/SDT-Q600). Samples are heated from 30 ℃. Final heating temperatures are carefully chosen to avoid emission of Li.

1.5 Rheology. Rheological experiments were carried out using a stress-controlled rheometer (Anton Paar MCR302) with a 25 mm parallel plate attachment. Frequency sweep test was conducted to characterize the dynamic moduli of the sample. In the experiments, a fixed strain of 0.1% was applied on the PCE sample. The frequency sweep was performed at temperatures at 70 °C and 30 °C, over a frequency range between 0.1 to 628 Hz. During the test, the sample was first heat to 70 ℃ and kept for 10 min to completely melt the PEO crystals. Then the gap between two parallel plates was set to 0.3 mm to compress the sample inbetween, and extra material was squeezed outside. Next it was quenched to 30 °C to crystallize isothermally for 16 h. To reduce the impact of shear history and thermal inhomogeneity, the experiment was carried out immediately after the thermal treatment.

1.5 Polarization experiments. The polarization experiments were operated with a Solartron Materials Testing System. The ionic transference number (T_{Li^+}) was measured by the AC

impedance spectroscopy and the DC polarization using Li | composite | Li symmetric cells. The applied polarization voltage was 500 mV. T_{Li^+} can be calculated according to[2]

$$T_{Li^+} = \frac{I_s(\Delta V - I_0 R_0)}{I_0(\Delta V - I_s R_s)} \quad \text{(S2)}$$

where ΔV is the polarization voltage, I_0 and R_0 are the initial current and resistance, and I_s and R_s are the steady-state current and resistance, respectively. The values T_{Li^+} for the composites are listed in Table S7.

2. Microstructure and composition of PCE

2.1 Nano CT Imaging

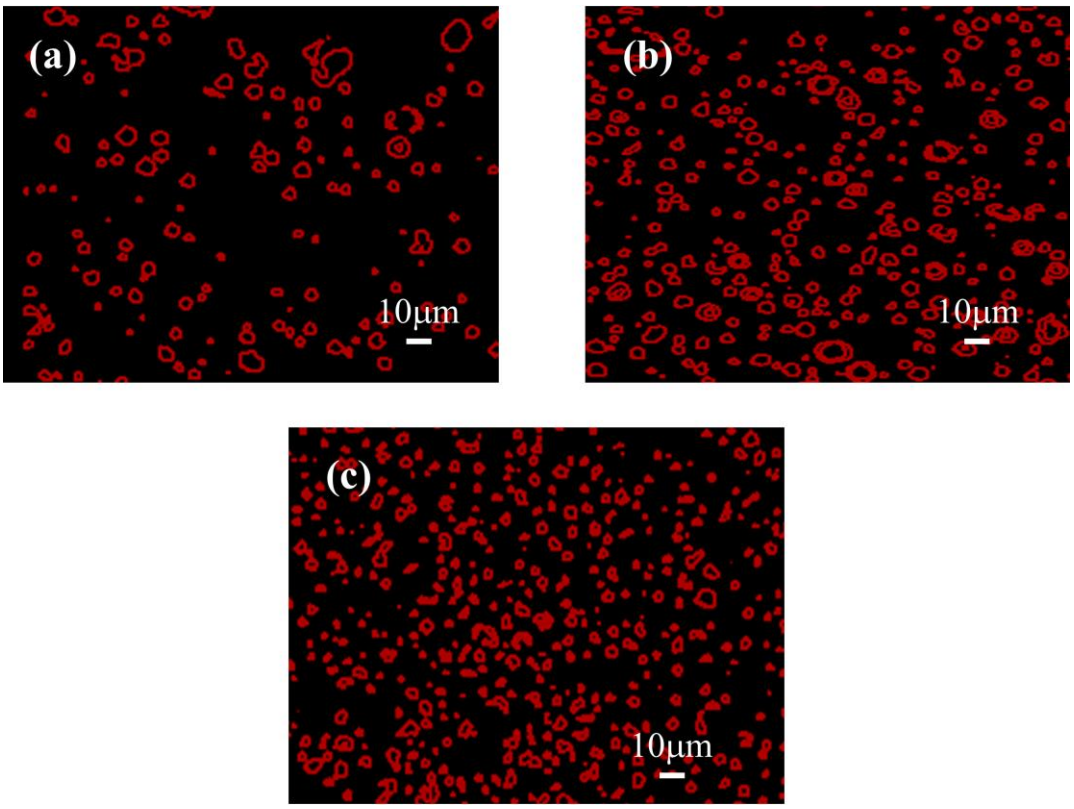

Figure S2. Cross sectional Nano CT images for PEO_{18}-$LiClO_4$ with 5 μm-SiO_2 particles dispersed in the matrix at *x* wt%, *x* = (a) 10, (b) 30 and (c) 70.

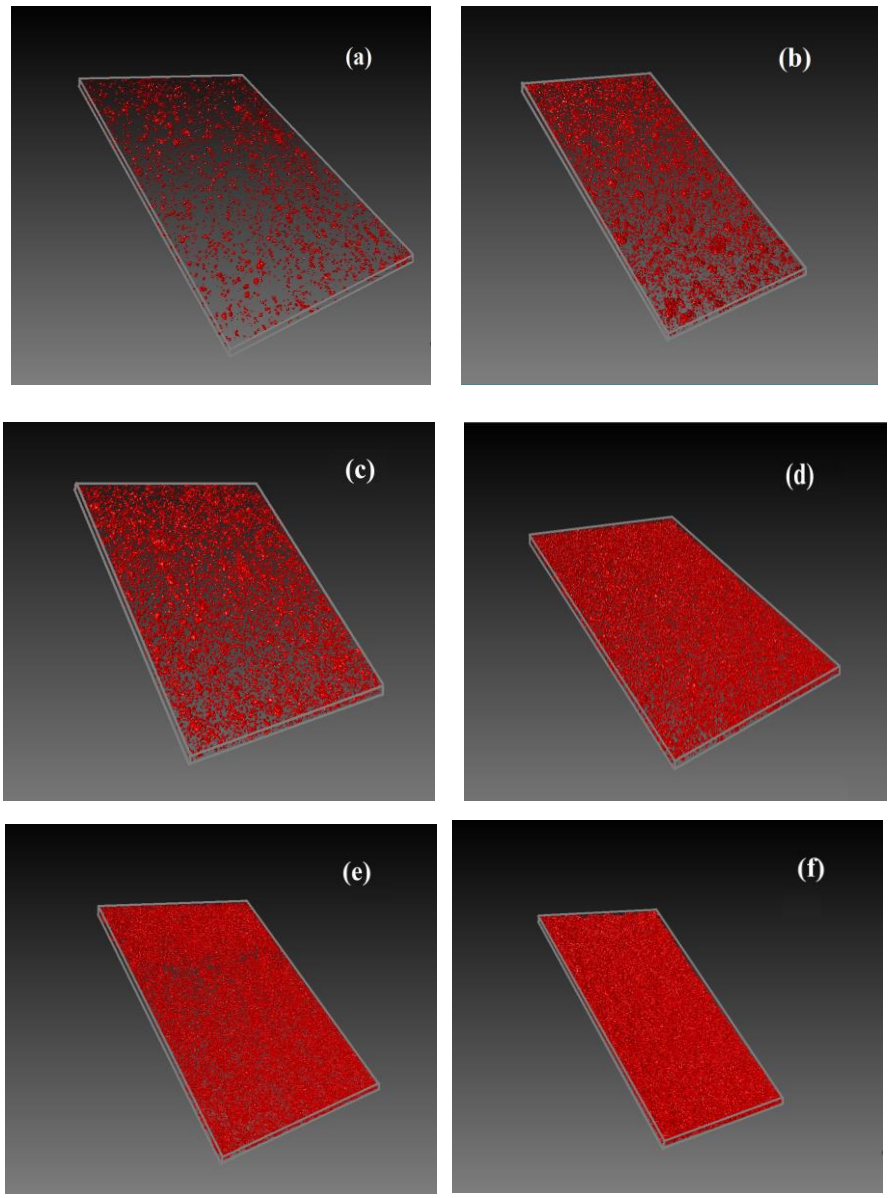

Figure S3. 3D Nano-CT images for PEO_{18}-$LiClO_4$-*x* wt % 5 μm-SiO_2, *x* = (a) 10, (b) 20, (c) 30, (d) 50, (e) 70 and (f) 80. SiO_2 particles are highlighted in red. The samples' planar dimensions are 600 μm × 500 μm in (a), (b), (c), and (d); 800 μm × 500 μm in (e); and 1000 μm × 500 μm in (f).

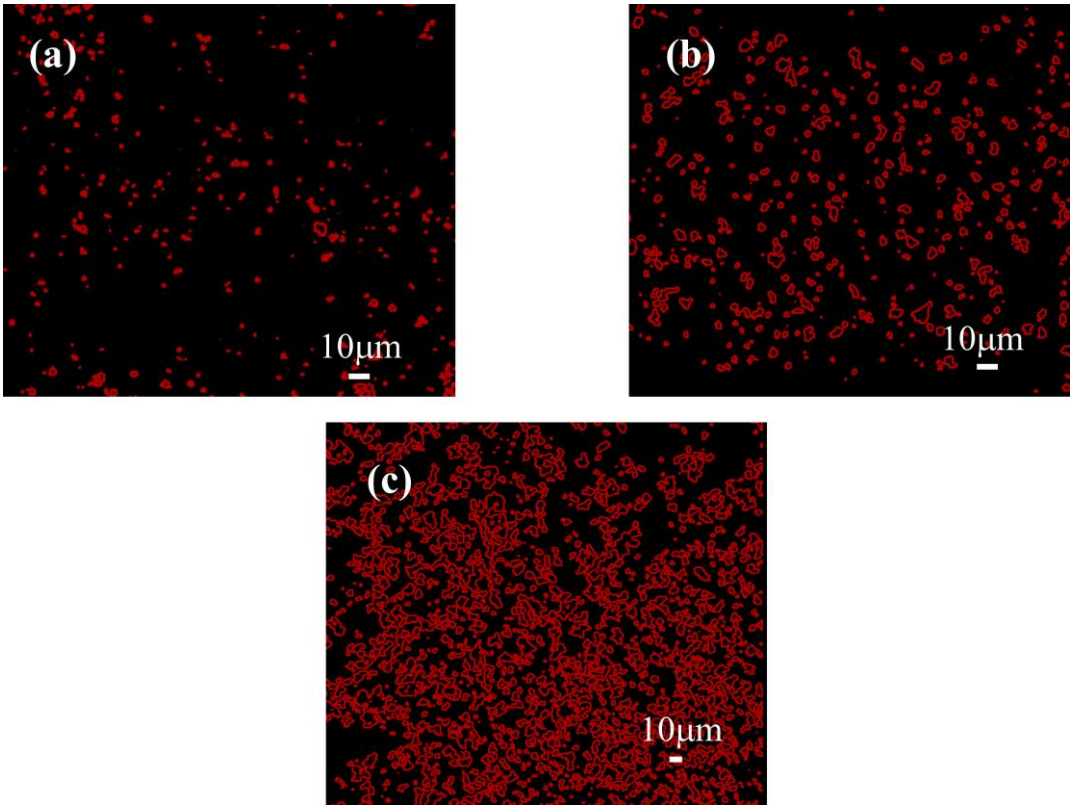

Figure S4. Cross sectional Nano CT images for PEO_{18}-$LiClO_4$ with 100 nm-SiO_2 particles dispersed in the matrix at *x* wt %, *x* = (a) 10, (b) 30 and (c) 70. It can be seen particle clusters are well dispersed in the composite.

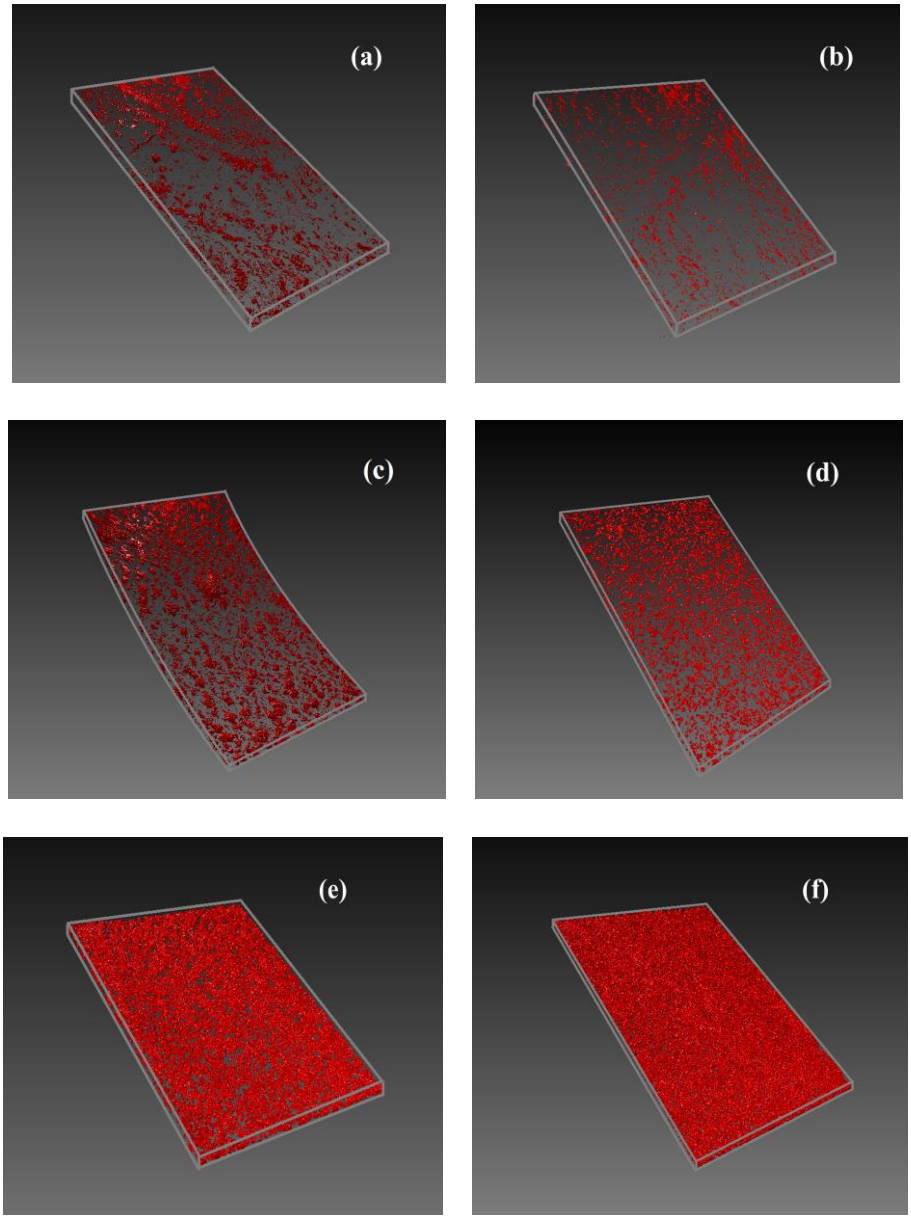

Figure S5. 3D Nano-CT images for PEO_{18}-$LiClO_4$-*x* wt % 100 nm-SiO_2, *x* = (a) 10, (b) 20, (c) 30, (d) 50, (e) 70 and (f) 80. The samples' planar dimensions are 1000 μm × 500 μm in (a) and (c); 600 μm × 500 μm in (b) and (e); and 800 μm × 500 μm in (d) and (f).

Table S1. Average particle/cluster size in composite electrolytes with various particle loadings.

5 μm-LLZTO		**500 nm-LLZTO**		**5 μm-SiO_2**		**100 nm-SiO_2**	
wt%	Particle size(μm)	wt%	Particle size(μm)	wt%	Particle size(μm)	wt%	Particle size(μm)
10	3	10	1.68	10	2.45	10	1.66
30	3.08	20	1.53	20	2.55	20	1.50
50	3.93	30	1.62	30	2.87	30	1.58
70	4.63	50	1.98	50	3.08	50	2.06
80	2.95	70	2.18	70	3.74	70	1.66
		80	2.08	80	2.54	80	2.21

2.2 TGA

Raw TGA thermogram data and their first-order derivative curves for PEO_{18}-$LiClO_4$ with different weight loadings of 500 nm-LLZTO and 5 μm-SiO_2 particles are shown in Figure S6 and S7, respectively. Samples are heated from 30 ℃ to 600 ℃. The final temperature is chosen to avoid emission of Li. The results show one decomposition temperatures around 415 ℃ which corresponds to decomposition of PEO[3]. An extra peak exhibiting around 330 ℃ for sample loaded with SiO_2 particles is due to different levels of Li^+ binding energy[4].

The red curve declines when heated from 30 ℃ to 100 ℃ which corresponds to water (a small amount of water was absorbed during sample transfer) evaporation, such as a, b, d, and e in Figure S6. The existence of water is because we sent the samples to elsewhere for measurements which took a short period with a chance for water absorption. However, this does not affect the determination of compositions of the samples. As a result, the measured weight percentage of particles is calculated from: $\mathrm{wt\%(measured)} = \frac{100\% - \mathrm{wt\%(H_2O)} - \mathrm{wt\%(PEO)}}{100\% - \mathrm{wt\%(H_2O)}}$.

As shown in Table S2, the nominal and measured particle loadings are quite close. For convenience, we use the nominal weight fraction to indicate the sample.

It should be noted that the purpose of TGA measurement is to confirm compositions of the samples. A small amount of water could be absorbed during sample transfer and shipping; however, water is strictly prevented in EIS and DRS measurements.

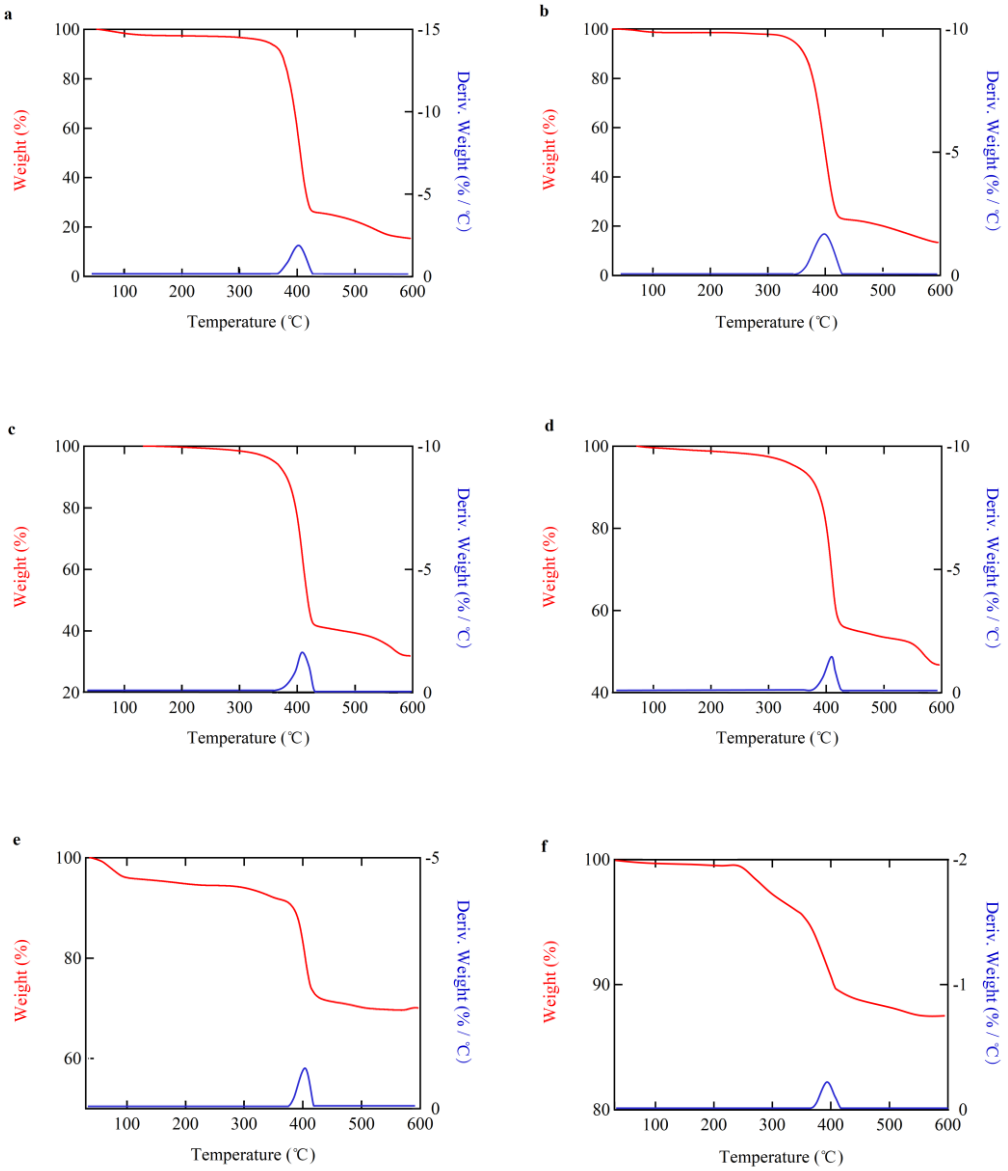

Figure S6. Decomposition curves for PEO_{18}-$LiClO_4$ with 500 nm-LLZTO particles dispersed in the matrix at *x* wt %, *x* = (a) 10, (b) 20, (c) 30, (d) 50, (e) 70 and (f) 80.

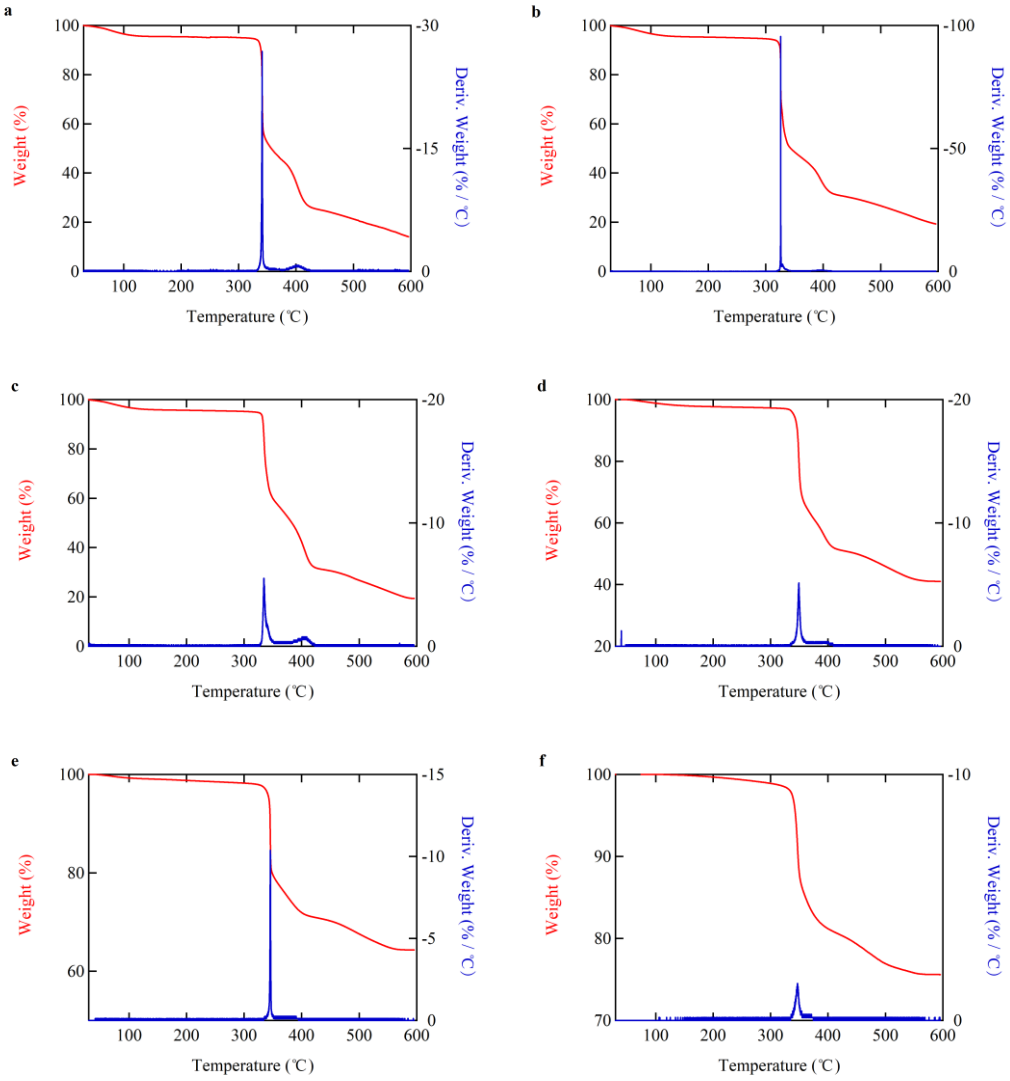

Figure S7. Decomposition curves for PEO_{18}: $LiClO_4$ with 5 μm-SiO_2 particles dispersed in the matrix at *x* wt %, *x* = (a) 10, (b) 20, (c) 30, (d) 50, (e) 70 and (f) 80.

Table S2. Measured weight percentage of loading particles from TGA.

5 μm-LLZTO		**500 nm-LLZTO**		**5 μm-SiO_2**		**100 nm-SiO_2**	
Nominal wt%	Measured wt%	Nominal wt%	Measured wt%	Nominal wt%	Measured wt%	Nominal wt%	Measured wt%
10	6	10	15	10	17	10	6
30	32	20	13	20	19	20	19
50	44	30	32	30	22	30	26
70	75	50	47	50	41	50	49
80	73	70	70	70	64	70	66
		80	88	80	76	80	78

2.3 FTIR

FTIR measurements were performed and the results showed no remaining solvent in the film and no water was absorbed during the sample preparation as shown in Figure S8. Water absorption leads to wide peaks at ~3500 cm^{-1} and peaks at 1631 cm^{-1} and 3465 cm^{-1}. No new peaks are observed in Figure S9 after addition of lithium salt and particles, which indicates no chemical reactions occur.

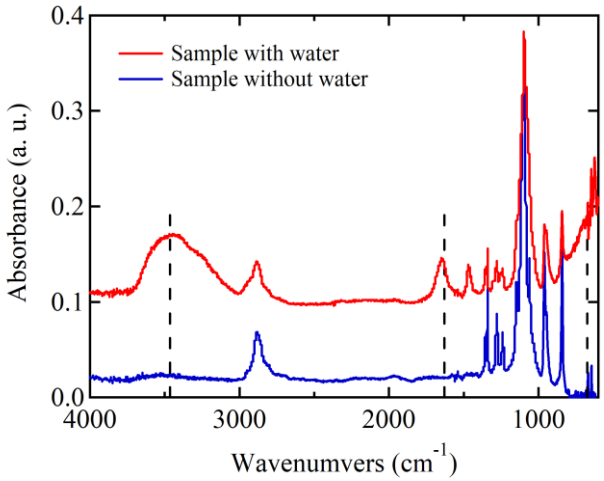

Figure S8. FTIR spectra for sample with and without water. The dash lines are absorption band for water.

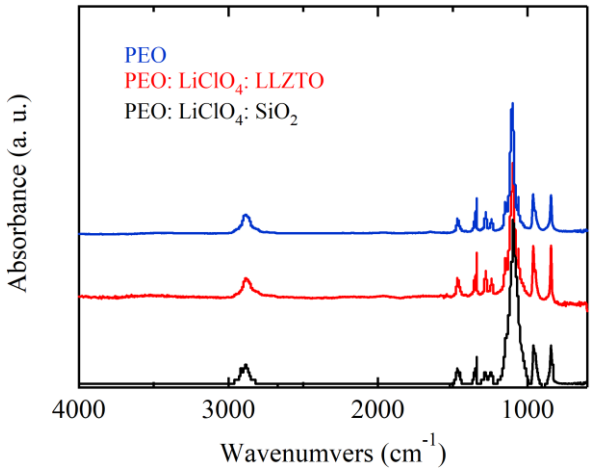

Figure S9. FTIR spectra for pure and composite samples.

3. Percolation theory

As the polymer matrix is partially conductive (in amorphous phases), the dimensions of the filler clusters influence the conformation of polymer chains and thus play an important role. When PCE is loaded with voltage, the ions move and accumulate near the boundaries. The diffusion of the ions results in formation of space charge layer and induces conductivity. Usually the conductivity is analyzed by percolation and effective medium theory in organic or inorganic composite materials[5-7]. The effective overall composite conductivity (σ_{m}) is given by

$$\sigma_{\mathrm{m}} = \sigma_{\infty}(\phi - \phi_{\mathrm{c}})^{\mathrm{t}} \tag{S3}$$

where ϕ is the mass fraction of filler, ϕ_c is the percolation threshold representing formation of continuous ionic pathway, and t is an exponent related to the dimension of percolation conductive networks[8]. Once the connected pathway is formed across the electrolyte membrane, increasing mass fraction of fillers could further increases σ_{m}. However, overabundant fillers usually agglomerate, and clustered fillers not only result in the loss of interphase volume but also obstruct the formation of a percolating network in the composite, identified as blocking effect[9, 10]. The trend is shown in Figure S8 below. Thereby a proper degree of separation of fillers, i.e., a high aspect ratio (η), is thought to be critical for a higher t and higher limit of ϕ. This is also found to be helpful in decreasing ϕ_{c} as $\phi_{\mathrm{c}} = 1/\eta$ (Ref. [11]).

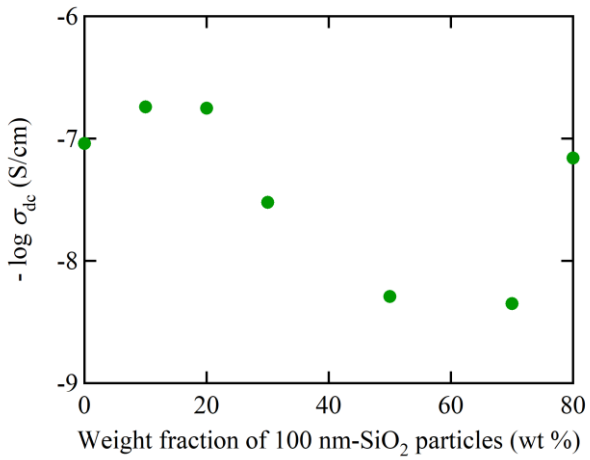

Figure S10. Weight fraction dependence of σ_{dc} in PEO_{18}: $LiClO_4$: 100 nm-SiO_2 at T = 30 ℃.

4. Crystallization behavior

In conventional polymer electrolytes, ion transport in crystalline phases is generally much lower than that in amorphous phases[12], because reduced segmental motion in the crystalline phases is greatly suppressed. Ion transport is generally facilitated by the segmental motion. Moreover, the coordination number, that is, the number of oxygen atoms bonded with Li/Li^+ is higher for amorphous PEO than crystalline PEO[4]. We note that there are reports claiming that ion conductivity in ordered environment of crystalline phase can be greater than that in the equivalent amorphous phase[13]. Formation of crystalline lamellae also leads to a high in–plane conductivity[14]. As we reported in our previous work[15], crystallization of PEO includes formations of both primary lamellar stack and thinner secondary lamellae between primary stacks. Their growth rates are influenced by T_c. Hence crystallization morphology can be changed by changing T_c. We here set T_c to 20 ℃, 30 ℃ and 50 ℃ and set crystallization period to 16 h. From Table S3 and Table S4, the total crystallinity X_ts are mostly very close at different T_cs. It is also worth noting that X_t stays identical after following dynamical measurements.

Table S3. X_t of PEO_{18}- $LiClO_4$ with 100 nm-SiO_2 particles with different weight loadings. The values are the average from three duplicates.

wt% of 100 nm-	**X_t (%)**		
SiO_2 particles	T_c = 20 ℃	T_c = 30 ℃	T_c = 50 ℃
0	37.0	40.0	39.0
10	31.0	30.8	32.0
20	43.2	41.8	45.6
30	36.3	29.0	31.0
50	45.0	45.8	41.6
70	27.5	30.3	25.6
80	28.1	27.0	20.1

Table S4. X_t of PEO_{18}- $LiClO_4$ with 500 nm-LLZTO particles with different weight loadings. The values are the average from three duplicates.

wt% of 500 nm-LLZTO particles	**X_t (%)**		
	T_c = 20 ℃	T_c = 30 ℃	T_c = 50 ℃
0	37.0	40.0	39.0
10	31.0	30.2	31.7
20	29.8	28.8	28.6
30	26.8	18.6	24.7
50	24.4	23.8	29.4
70	33.2	33.2	32.7
80	44.0	43.7	42.7

Moreover, the existence of primary and secondary crystallization is linked to primary and secondary α processes, which are related to globally free and locally constrained dynamics of PEO chains[16]. Therefore, we think by changing T_c, we can modify conductivity performance by influencing segmental movements.

Conductivity and dynamical properties induced by different T_cs are listed in Table S5 and S6 below. T_c does influence the dynamics but its impact is lower than weight fraction of the fillers. As such, we selected a single T_c of 30 ℃, the samples for further characterization were prepared with an isothermal crystallization at 30 ℃ for a certain period of 16 h.

Table S5. Conductivity and relaxation time of PEO_{18}- $LiClO_4$- *x* wt% 100 nm-SiO_2 (*x* = 30, 70) at 30 ℃.

wt% of 100 nm-SiO_2 particles	**T_c (℃)**	**log σ_{dc} (S/cm)**	**τ_{inter} (s)**	**τ_α (s)**	**$\tau_{\alpha 2}$ (s)**
30	20	-6.9	2.1×10^{-3}	3.6×10^{-6}	N/A
	30	-7.5	5.0×10^{-3}	3.8×10^{-6}	2.1×10^{-5}
	50	-6.7	7.0×10^{-4}	1.4×10^{-6}	6.2×10^{-6}
70	20	-8.1	4.5×10^{-2}	5.1×10^{-6}	2.5×10^{-5}
	30	-7.9	2.5×10^{-2}	5.3×10^{-6}	3.3×10^{-5}
	50	-7.2	2.5×10^{-2}	5.0×10^{-6}	2.5×10^{-5}

Table S6. Conductivity and relaxation time of PEO_{18}- $LiClO_4$- *x* wt% 500 nm-LLZTO (*x* = 20, 70) at 30 ℃.

wt% of 500 nm-LLZTO particles	T_c (℃)	log σ_{dc} (S/cm)	τ_{inter} (s)	τ_{α} (s)	$\tau_{\alpha 2}$ (s)
20	20	-6.4	9.3×10^{-3}	2.5×10^{-6}	1.0×10^{-4}
	30	-6.6	6.5×10^{-3}	2.4×10^{-6}	1.2×10^{-4}
	50	-6.3	3.1×10^{-3}	2.5×10^{-6}	7.9×10^{-5}
70	20	-6.7	7.7×10^{-1}	3.3×10^{-6}	2.0×10^{-4}
	30	-7.2	9.5×10^{-1}	3.3×10^{-6}	2.1×10^{-4}
	50	-7.4	8.4×10^{-1}	3.2×10^{-6}	1.4×10^{-4}

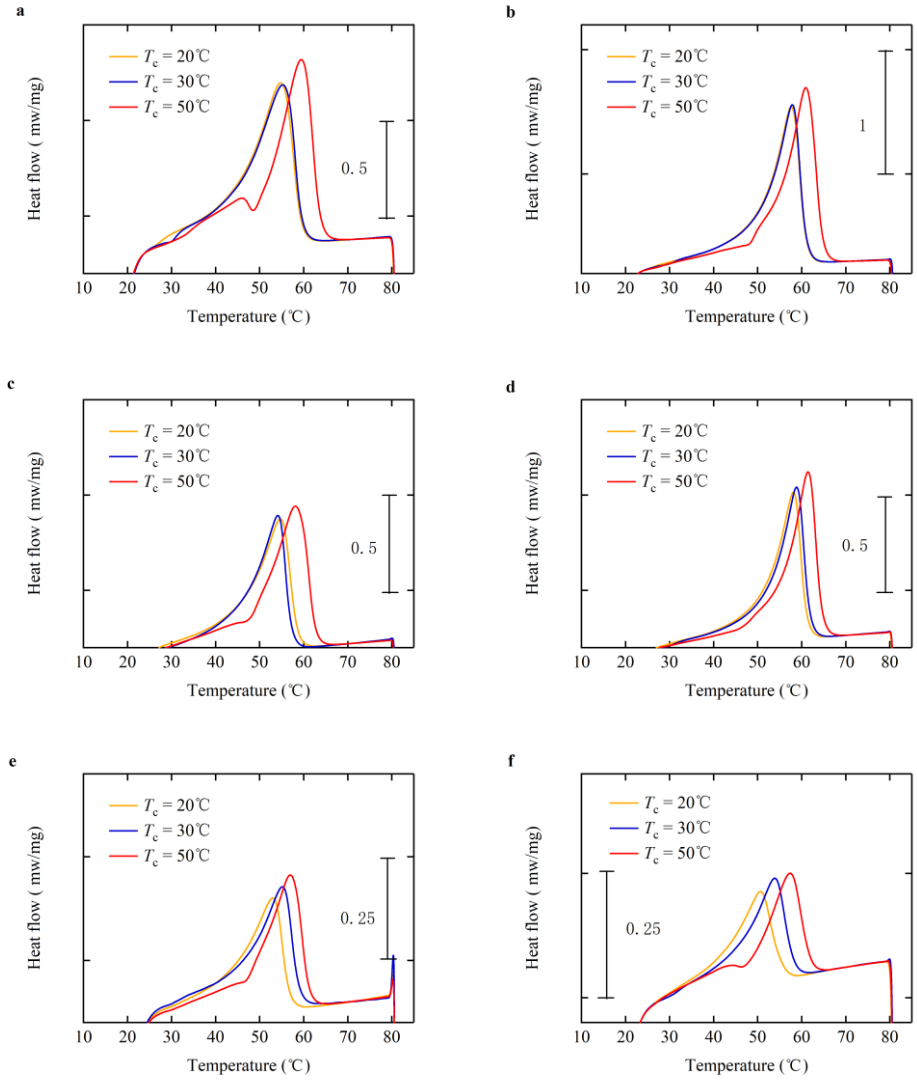

Figure S11. DSC endothermic traces for PEO_{18}- $LiClO_4$ with 100 nm-SiO_2 particles dispersed in the matrix at *x* wt % as a function of temperature. *x* = (a) 10, (b) 20, (c) 30, (d) 50, (e) 70 and (f) 80.

5. Mechanical characterization

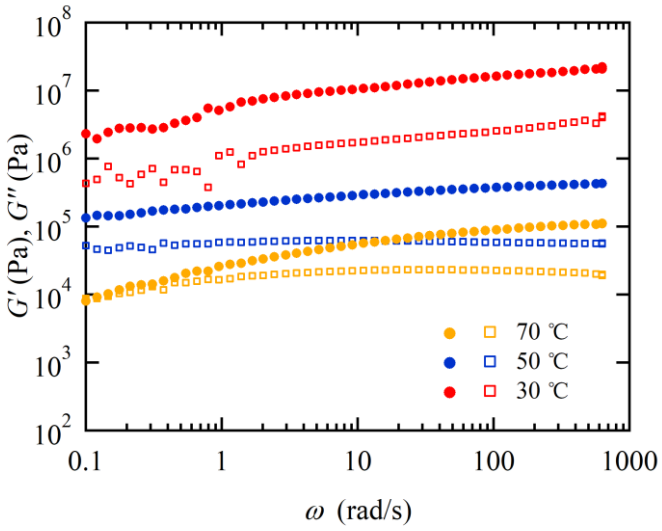

Figure S12. Shear moduli of PEO_{18}- $LiClO_4$- 5 wt% DEGDME at different temperatures. Filled circles and open squares represent the storage modulus *G'* and loss modulus *G"*, respectively. As PEO is semi-crystalline, samples in the first case are kept at 70 ℃ for 10 min to ensure complete melting of the crystals to obtain the mechanical response of amorphous PEO. At other temperatures, samples are crystallized at 30 ℃ for 16 h to ensure fully development of crystals.

6. Li^+ transference number

During polarization experiments, the current shows a sharp decrease at first and then level off. The fall in the current is due to two processes:

1) The growth at the electrodes of passivating layers;

2) The establishment of ions concentration gradient which reflected ion motions.

The effect is also observed in the a.c. measurements as shown in the inset.

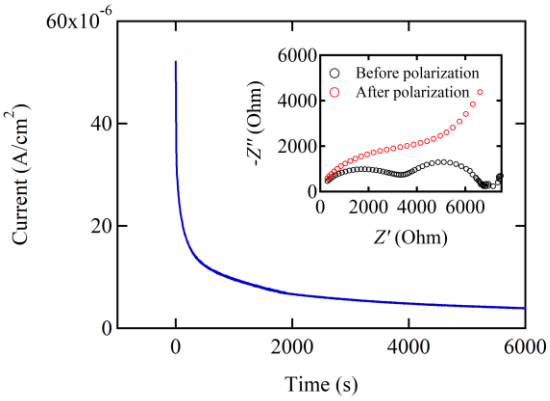

Figure S13. Current evolution under a polarization voltage of 500 mV. The inset shows the impedance spectra of Li | PEO_{18}: $LiClO_4$ | Li cell at 30 ℃.

Table S7. Ionic transference numbers (T_{Li^+}) from analysis of polarization experiments.

Sample ID	I_0 (μA)	I_s (μA)	R_0 (Ω)	R_s (Ω)	T_{Li^+}	log σ_{dc} (S/cm)
#1	42	16	802	873	0.37	-5.8
#2	597	392	4	39	0.67	-2.9
#3	35	11	201	1428	0.32	-4.5

#1: PEO_{18}- $LiClO_4$- 10 wt% DEGDME, #2: PEO_{18}- $LiClO_4$- 10 wt% 500 nm-LLZTO: 5 wt% DEGDME, #3: PEO_{18}- $LiClO_4$- 30 wt% 500 nm-LLZTO: 5 wt% DEGDME.

7. Dynamics

7.1 Identification of region boundaries

Identification for existence of MWS process is critical, as sometimes it is ignored and mistakenly recognized as EP. Polarization processes can be discriminated by analyzing their dominant regions[17]. Their relative regions are determined by second derivative of ε_r'. From high to low frequency, MWS is between the first and second local maximums, while EP is between the second local maximum to second local minimum. The example sample is shown below where the first derivative of ε_r' is got from $\partial(\log \varepsilon_r^{'}) / \partial(\log f)$ and second derivative of ε_r' is from $\partial(\log \varepsilon_r^{'})^2 / \partial(\log f)^2$.

Existence of MWS can also be observed via $\tan\delta$ curve as shown in Figure S13. The $\tan\delta$ curve can be decomposed into two processes which show separated peaks exceeding 1.

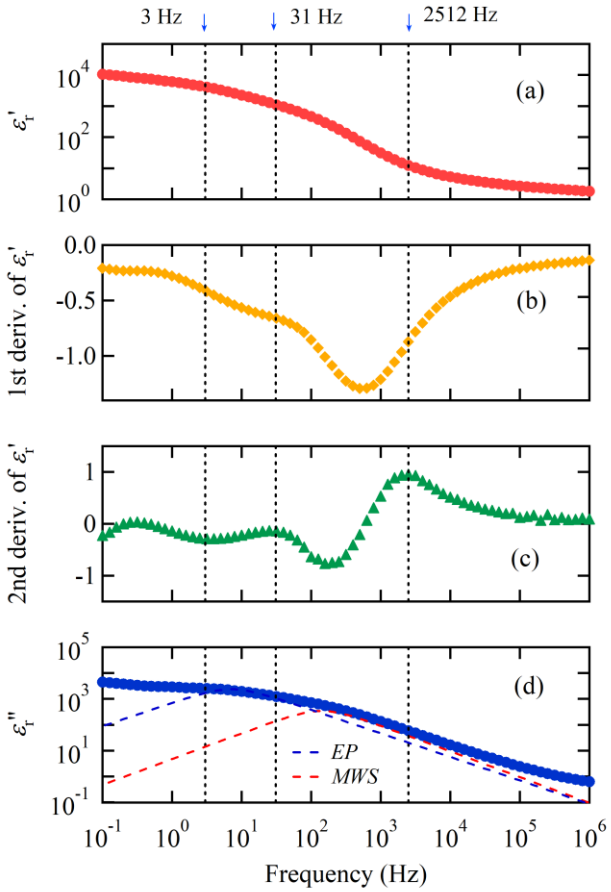

Figure S14. Real part ε_r' **(a)** and imaginary part ε_r'' **(d)** of the dielectric permittivity. **(b)** & **(c)** are the 1st and 2nd derivatization of ε_r'. Data are measured at 10 °C, for the sample of PEO_{18}:$LiClO_4$ with 100 nm-SiO_2 particles dispersed in the matrix at 10 wt%. The existence of MWS process and EP are indicated from (c).

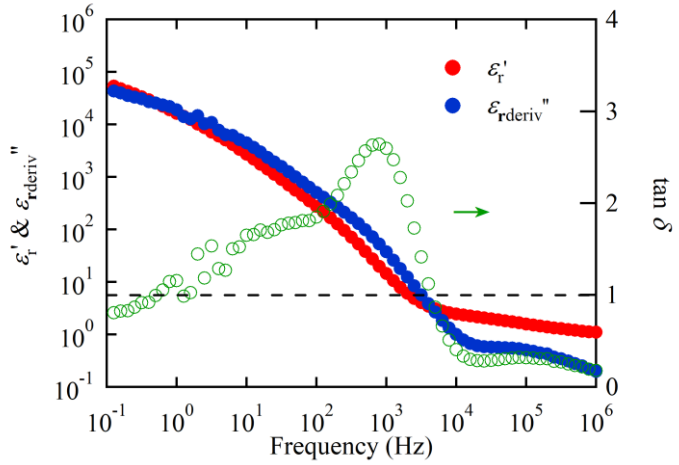

Figure S15. Dielectric spectrum for PEO_{18}: $LiClO_4$ with 500 nm-LLZTO particles dispersed in the matrix at 20 wt%.

7.2 Fitting procedures

Since lithium ions are in coordinating with ether oxygen atoms on PEO chains, Ohmic conduction shows up together with segmental movements above the glass-transition temperature. It may obscure loss peaks of α_2 process. Therefore first of all, the ohmic-conduction free loss was got from Equation (8) as shown in Figure S14a. $\varepsilon''_{\mathbf{rder}}$ is further used to extract relaxation time of α, α_2 and β process according to Equation (9). In our cases b is set to 1 as interpreted in our previous paper.[15] Low frequency tail is corresponded to narrower MWS process.[18] Then ε''_{σ} was determined from $\varepsilon''_{\mathrm{r}} - \varepsilon''_{\mathrm{rder}}$ in the range where it varies linearly with the frequency as displayed in Figure S14b. Since the Ohmic conduction is originated from hopping conduction, a hop of a charge carrier to a new site is successful only when the outer field frequencies is lower than $1/\tau_{\sigma}$. Otherwise it will jump back with a high probability.[19] The limit τ_{σ} can be estimated by

$$\tau_{\sigma} = \frac{\varepsilon_0 \varepsilon_{\mathrm{s}}}{\sigma_{\mathrm{dc}}} \tag{S4}$$

With decreasing frequency, propagation of charges fails as charges tend to separate and blocked at interfaces. This is the reason why Ohmic conduction shows up in a limited range. Finally, by sum of relaxation process as written in Equation (11), the rest parameters $\Delta\varepsilon$, a, b, m are got from raw dielectric loss data.

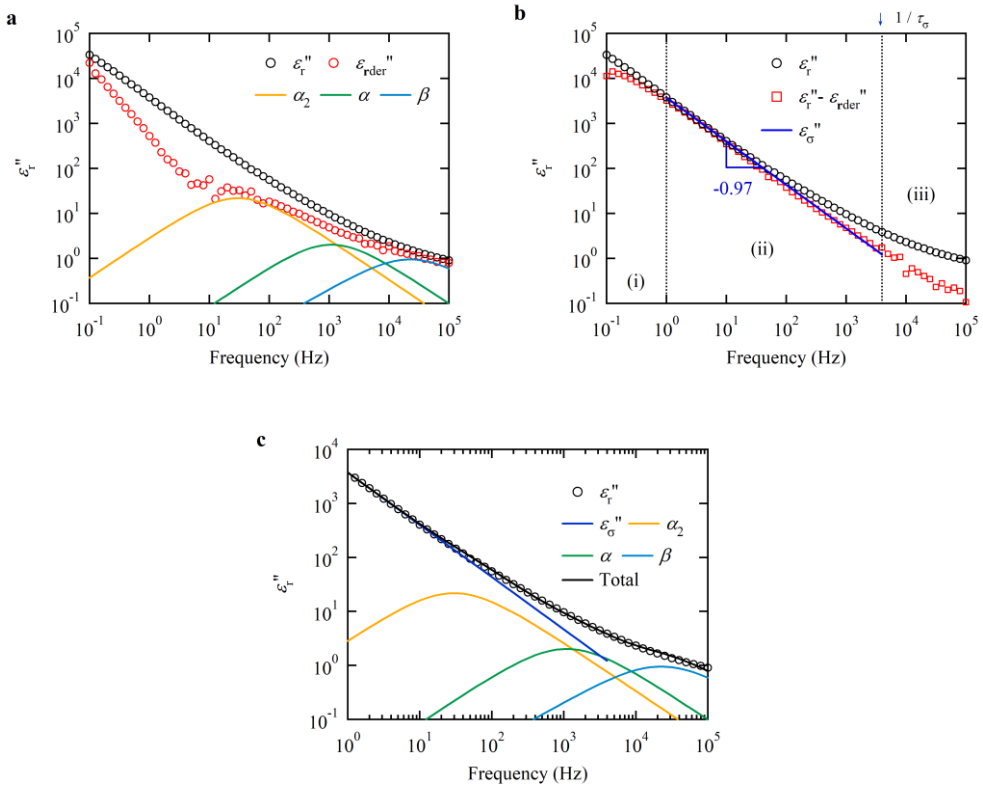

Figure S16. Representative loss dielectric spectra to show fitting procedures. **(a)** Rough decomposition of loss spectra from $\varepsilon''_{\mathrm{rderiv}}$. **(b)** Ohmic conduction contribution in the range where it varies linearly with frequency. (i) (ii) and (iii) represent different origin of loss spectra: charges separation at interfaces, charges propagation, and dipoles fluctuations respectively. **(c)** Refined decomposition of loss spectra. Data are measured at -30 ℃ of PEO_{18}-$LiClO_4$-10 wt% DEGDME.

7.3 Correlation between Z^* and ε^*

Equations for generating Nyquist plot from dielectric permittivity:

$$\varepsilon^*(\omega) = \frac{1}{i\omega Z^*(\omega) C_0} \tag{S5}$$

$$\text{Right} = \frac{-i}{\omega C_0 (Z' - \mathrm{i}Z'')} = \frac{-i(Z' + \mathrm{i}Z'')}{\omega C_0 |Z|^2} = \frac{-iZ'}{\omega C_0 |Z|^2} + \frac{Z''}{\omega C_0 |Z|^2} \tag{S6}$$

$$\text{Left} = \varepsilon' - i\varepsilon'' \tag{S7}$$

$$\therefore \varepsilon' = \frac{Z''}{\omega C_0 |Z|^2}, \varepsilon'' = \frac{Z'}{\omega C_0 |Z|^2} \tag{S8}$$

7.4 Sensitivity of relaxation time to conductivity

The characteristic times of a dynamic process are related to σ_{dc}. Higher conductivity is accompanied by lower τ. Influence of DEGDME is higher for samples with 5um-LLZTO particles.

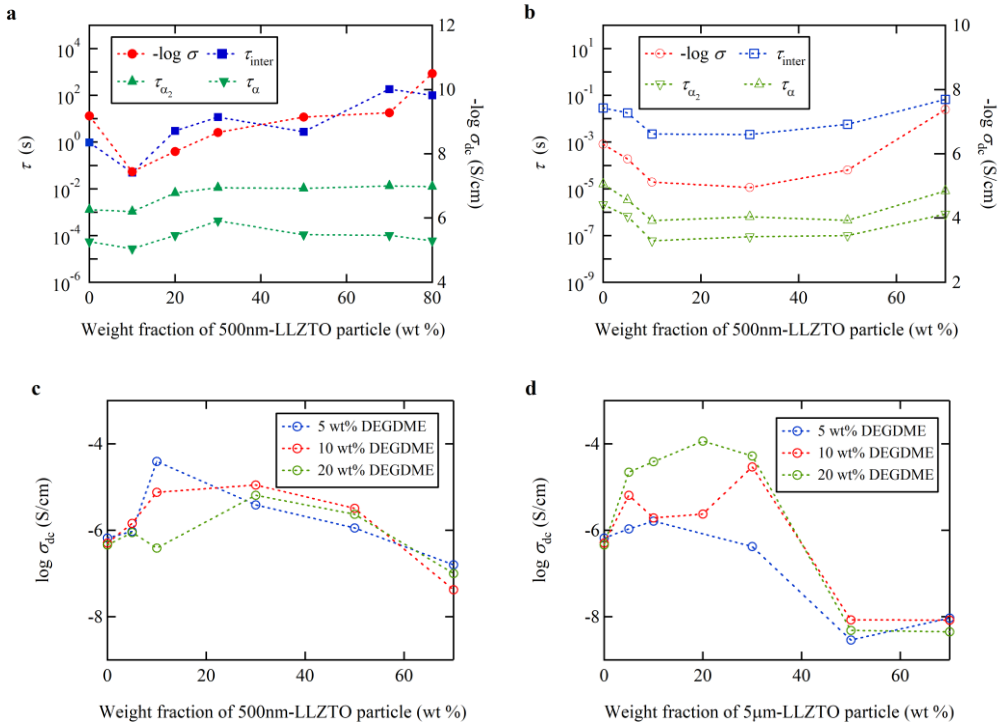

Figure S17. τ_{inter}, τ_{α}, τ_{α_2} and $-\log\sigma$ versus weight fraction of 500 nm-LLZTO **(a)** without and **(b)** with DEGDME addictive at 10 wt%, T = 17 °C. **(c)** 500nm-LLZTO dependent conductivities. **(d)** 5μm-LLZTO dependent conductivities.

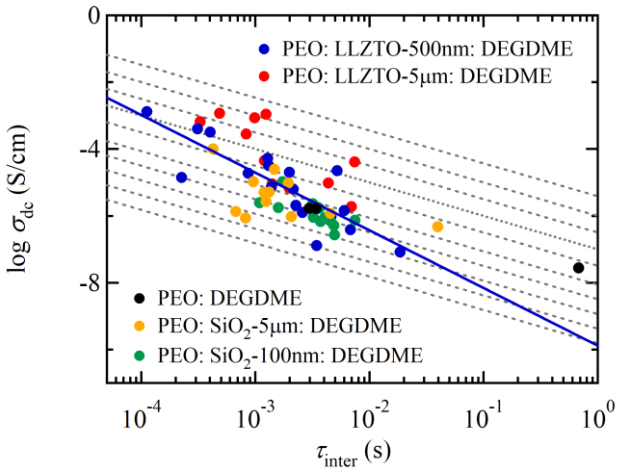

Figure S18. The dc conductivity versus relaxation rime of the MWS process. Slope of grey dash lines are -1 obtained from log σ= -logτ_{inter}+ log($\varepsilon_0\varepsilon_s^2/\varepsilon_\infty$), while that of the blue line is -1.7.

7.5 VFT plots

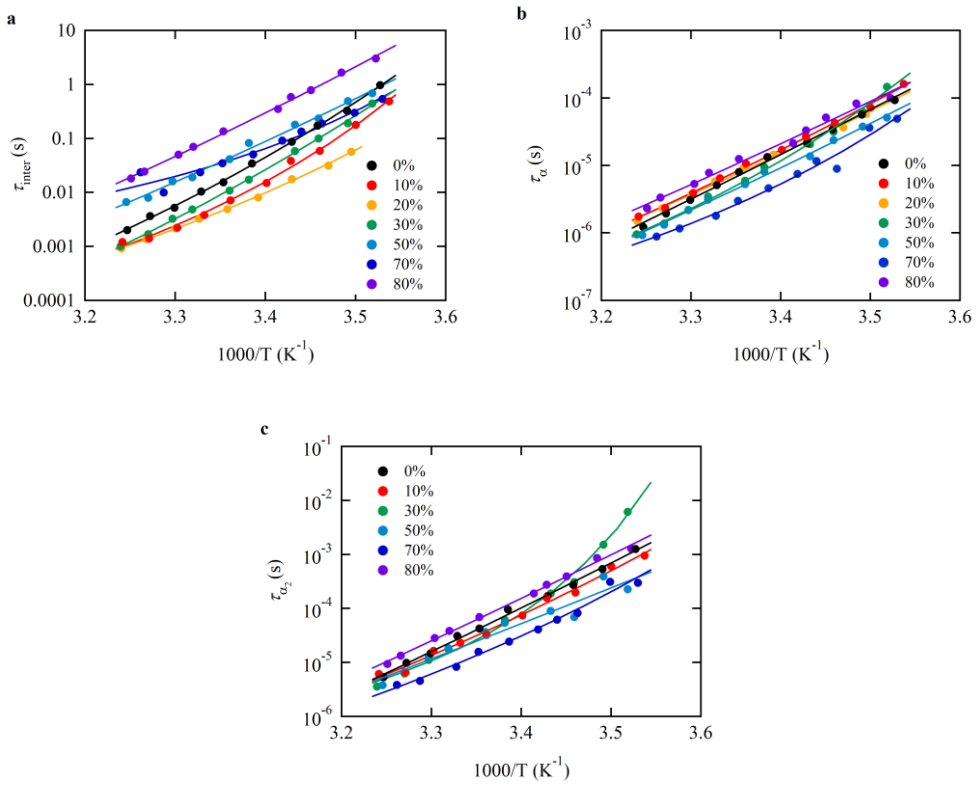

Figure S19. Temperature dependence of the characteristic time **(a)** τ_{inter}, **(b)** τ_{α} and **(c)** $\tau_{\alpha 2}$ of PEO_{18}-$LiClO_4$-100 nm-SiO_2 at various weight percent. Lines through the data points are fits from the VFT equation.

Table S8. Results from fits to the VFT equation for PEO_{18}- $LiClO_4$- *x* wt% 100 nm - SiO_2.

wt% of 100 nm-SiO_2	MWS			α			α_2		
	B(K)	T_0(K)	ln(τ_0) (s^{-1})	B(K)	T_0(K)	ln(τ_0) (s^{-1})	B(K)	T_0(K)	ln(τ_0) (s^{-1})
0	2213	201	-27	11120	43	-55	8757	94	-53
10	747	239	-18	3747	148	-37	2734	180	-33
20	1118	218	-19	4743	124	-39		N/A	
30	3096	184	-32	976	225	-26	286	263	-19
50	5031	138	-35	4779	127	-40	10050	54	-52
70	384	245	-11	655	233	-23	1455	209	-28
80	4982	143.8	-34	5505	111	-41	9101	86.88	-53

7.6 Supplementary data of α_2 process

This part shows supplementary data for Figure 4 and 5 in the article.

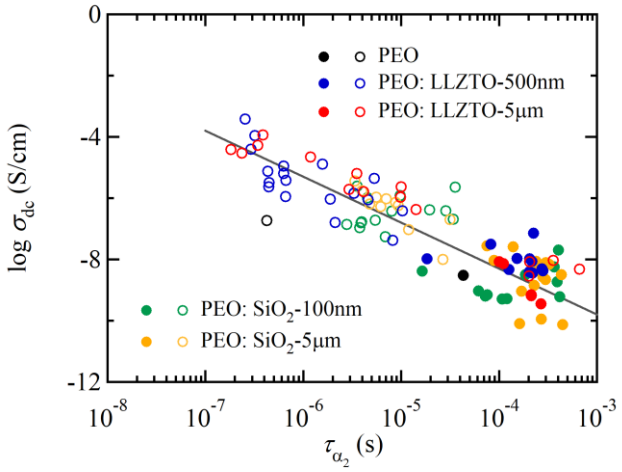

Figure S20. Conductivity versus relaxation time of the α_2 process at T = 17 °C. Closed and open symbols represent samples without and with DEGDME plasticizer, respectively. DEGDME addition accelerates τ_{α_2}.

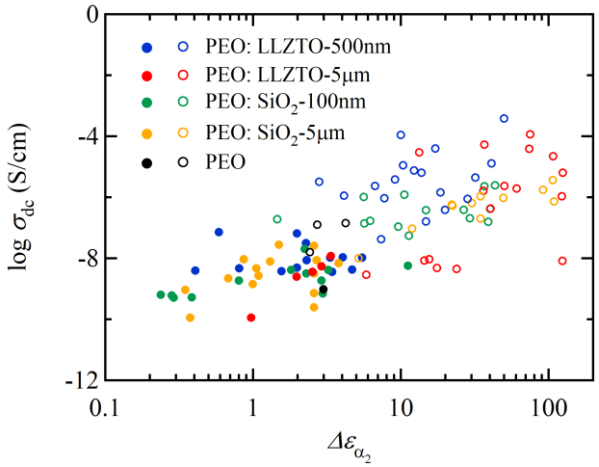

Figure S21. Ionic conductivity versus dielectric strength of α_2 process at T = 17 ℃. Closed and open symbols represent samples without and with DEGDME plasticizer, respectively.

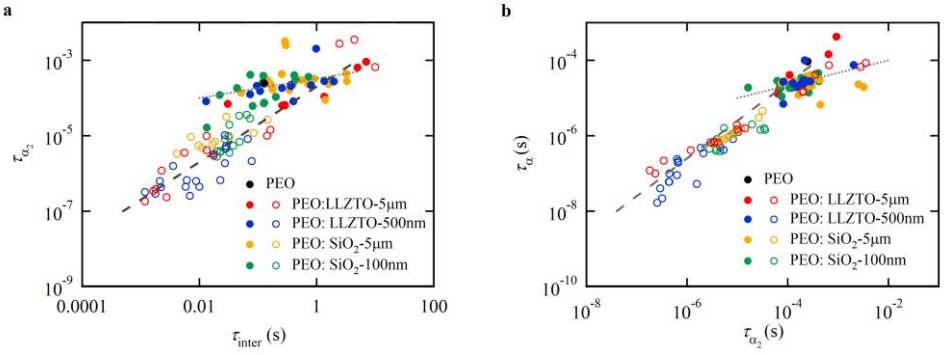

Figure S22. τ_{α_2} versus τ_{inter} (a), and τ_{α} versus τ_{α_2} (b). The closed and open circles represent samples without and with DEGDME addition, respectively. All data in this figure are measured at 17 ℃.

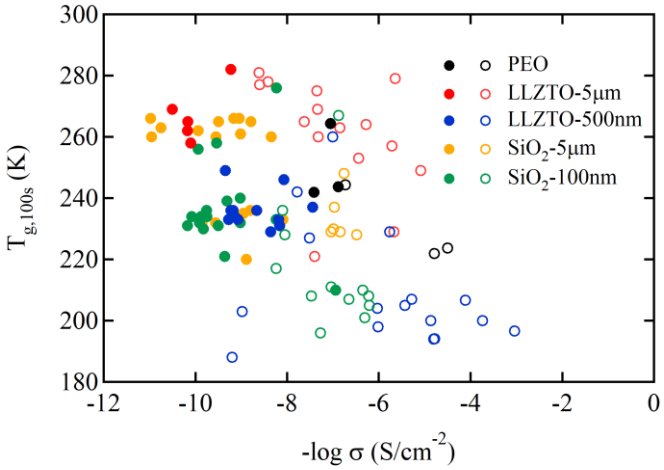

Figure S23. $T_{g,100s}$ versus ionic conductivity. The closed and open circles represent samples without and with DEGDME addition, respectively. Increasing conductivity is correspond to decrease in T_g. $T_{g,100s}$ is determined as the temperature where the relaxation time of α process is 100 s.

7.7 Coupling between relaxation processes

Ionic conductivity in a polymer is observed to be coupled with characteristic time τ of relaxation process, $\sigma\tau T = \tau^{\mu}$, where μ is the decoupling degree between two processes. Here τ represents one from τ_{inter}, τ_{α}, τ_{α_2}. An example of PEO_{18}- $LiClO4$ with 500 nm-LLZTO particles is shown in Figure S22.

The decoupling degrees for different particles are shown in Table S9. For same process, μ is not influenced by weight loading or particle type.

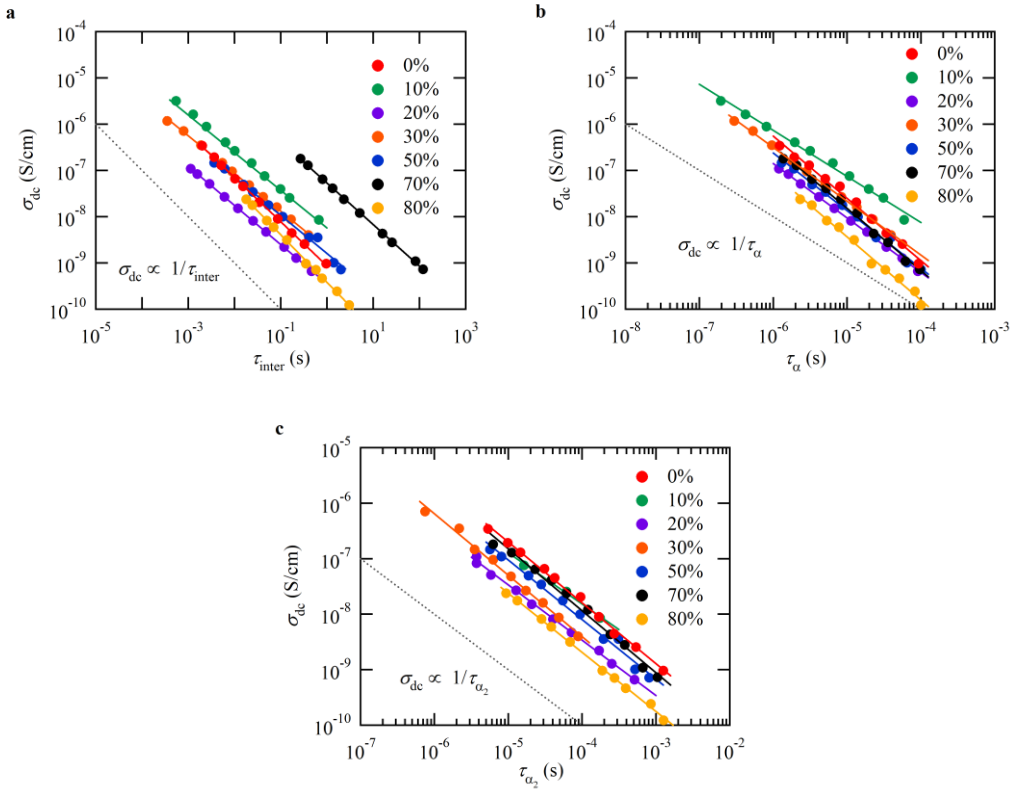

Figure S24. Coupling phenomenon for **(a)** MWS, **(b)** α and **(c)** α_2 process for PEO_{18}-$LiClO_4$ with 500 nm-LLZTO particles dispersed in the matrix when T_c = 30 °C. Solid lines are fitted by $\sigma\tau T = \tau^{\mu}$. Schematic dotted lines show relaxation processes which are fully coupled with conductivity, i.e., μ = 0.

Table S9. Decoupling degree μ for 500 nm-LLZTO (denoted by "L")and 100 nm-SiO_2 (denoted by "S") samples, T_c = 20 ℃.

wt%	MWS		α		α_2	
	L	S	L	S	L	S
0	0.05		-0.3		-0.09	
10	0.19	-0.10	0	-0.3	0.10	0.16
20	0.16	0.02	-0.20	-0.20	0	0.17
30	0.19	0.03	-0.20	-0.20	-0.10	0.18
50	0.18	0	-0.20	-0.20	-0.10	-0.10
70	0.11	-0.10	-0.30	0.03	-0.10	0.16
80	0.13	-0.20	-0.30	0.03	-0.10	0.18

Table S10. Activation energy barrier for PEO_{18}- $LiClO_4$: *x* wt% SiO_2 without and with DEGDME addition.

wt%	Without		With	
	MWS	α	MWS	α
20	4415	6539	663	7616
50	4523	5250	947	3018
70	4775	5086	433	3220
80	4016	6237	3099	6488

REFERENCES

1. Wu, X.-L.; Xin, S.; Seo, H.-H.; Kim, J.; Guo, Y.-G.; Lee, J.-S., Enhanced Li^+ conductivity in PEO-LiBOB polymer electrolytes by using succinonitrile as a plasticizer. *Solid State Ion.* **2011,** *186*, 1-6.

2. Evan, J.; Vincent, C. A.; Bruce, P. G., Electrochemical measurement of transference numbers in polymer electrolytes. *Polymer* **1987,** *28*, 2324−2328.

3. Pakravan, M.; Heuzey, M. C.; Ajji, A., Core-shell structured PEO-chitosan nanofibers by coaxial electrospinning. *Biomacromolecules* **2012,** *13*, 412-21.

4. Das, D.; Chandrasekaran, A.; Venkatram, S.; Ramprasad, R., Effect of crystallinity on Li adsorption in polyethylene oxide. *Chem. Mater.* **2018,** *30*, 8804−8810.

5. Yamada, H.; Bhattacharyya, A. J.; Maier, J., Extremely high silver ionic conductivity in composites of silver halide (AgBr, AgI) and mesoporous alumina. *Adv. Funct. Mater.* **2006,** *12*, 525–530.

6. Li, Z.; Huang, H.-M.; Zhu, J.-K.; Wu, J.-F.; Yang, H.; Wei, L.; Guo, X., Ionic conduction in composite polymer electrolytes: Case of PEO:Ga-LLZO composites. *Appl. Mater. Interfaces* **2019,** *11*, 784−791.

7. Wieczorek, W.; Such, K.; Florjanczyk, Z.; Stevens, J. R., Polyether, polyacrylamide, $LiClO_4$ composite electrolytes with enhanced conductivity. *J. Phys. Chem.* **1994,** *98*, 6840-6850.

8. Zhang, P.; Wang, B.-b.; Xia, Q.-j.; Zou, J., Study on the effect of tailoring the segmented PU molecules on electrically conductive properties and percolation threshold of PU/MWCNTs nanocomposites. *Synthetic Metals* **2020,** *261*, 116300.

9. Maier, J., Ionic conduction in space charge regions. *Prog. Solid St. Chem.* **1995,** *23*, 171-263.

10. Qiao, R.; Deng, H.; Putz, K. W.; Brinson, L. C., Effect of particle agglomeration and interphase on the glass transition temperature of polymer nanocomposites. *J. Polym. Sci. B* **2011,** *49*, 740–748.

11. Bauhofer, W.; Kovacs, J. Z., A review and analysis of electrical percolation in carbon nanotube polymer composites. *Compos. Sci. Technol.* **2009,** *69*, 1486–1498.

12. Stainer, M.; Hardy, L. C.; Whitmore, D. H.; Shriver, D. F., Stoichiometry of formation and conductivity response of amorphous and crystalline complexes formed between poly(ethylene oxide) and ammonium salts: $PEO_x \cdot NH_4SCN$ and $PEO_x \cdot NH_4SO_3CF_3$. *Electrochem. Soc.* **1984,** *31*, 784-790.

13. Gadjourova, Z.; Andreev, Y. G.; Tunstall, D. P.; Bruce, P. G., Ionic conductivity in crystalline polymer electrolytes. *Nature* **2001,** *412*, 520-523.

14. Cheng, S.; Smith, D. M.; Li, C. Y., How does nanoscale crystalline structure affect ion transport in solid polymer electrolytes. *Macromolecules* **2014,** *47*, 3978–3986.

15. Huang, Y.; Ma, M.; Guo, Y., Melt crystallization and segmental dynamics of poly(ethylene oxide) confined in a solid electrolyte composite. *J polym Sci* **2020,** *58*, 466–477.

16. Fragiadakis, D.; Runt, J., Microstructure and dynamics of demicrystalline poly(ethylene oxide) −poly(vinyl acetate) blends. *Macromolecules* **2010,** *43*, 1028-1034.

17. Samet, M.; Levchenko, V.; Boiteux, G.; Seytre, G.; Kallel, A.; Serghei, A., Electrode polarization vs. Maxwell-WagnerSillars interfacial polarization in dielectric spectra of materials: Characteristic frequencies and scaling laws. *J. Chem. Phy.* **2015,** *142*, 194703.

18. van Turnhout, J.; Wübbenhorst, M., Analysis of complex dielectric spectra. II: Evaluation of the activation energy landscape by differential sampling. *J. Non-Cryst. Solids* **2002,** *305*, 50-58.

19. Debye, P.; Falkenhagen, H., Dispersion of the conductivity and dielectric constants of strong electrolytes. *Phys. Z.* **1928,** *29*, 121.